Single-Source Precursor to Complex Metal Oxide Monoliths with Tunable Microstructures and Properties: The Case of Mg-Containing Materials

Lu Zou, Xu Xiang, Jun Fan, and Feng Li*

*State Key Laboratory of Chemical Resource Engineering, Beijing University of Chemical Technology,
P.O. Box 98, Beijing 100029, P. R. China*

Received August 15, 2007. Revised Manuscript Received October 16, 2007

Synthesis of complex metal oxide monoliths ($MgAl_2O_4$, $MgFe_2O_4$, and $In_{2-x}Mg_xO_3$) with macropore frameworks through a novel single-source inorganic precursor route is successfully established. The synthesis approach mainly involves the formation of two-phase composite (desired complex metal oxide and MgO phases) monoliths induced by high-temperature sintering of layered double hydroxide (LDH) precursors, followed by a selective leaching of self-generated MgO sacrificial template from the sintered two-phase composites. The materials have been characterized by X-ray diffraction (XRD), Fourier transform infrared (FT-IR), thermogravimetric and differential thermal analysis (TG-DTA), scanning electron microscopy (SEM), and energy dispersive X-ray spectrometry (EDX). The results indicate that the microstructures (morphologies, particle sizes, spacing among particles, and compositions) of resultant macroporous monoliths could be finely tuned by changing precursor compositions and sintering temperatures of precursors. Further investigation shows that these as-prepared monoliths display promising surface superhydrophobicity for organically modified $MgAl_2O_4$ spinels, ferromagnetism for $MgFe_2O_4$ ferrites, and semiconductor optical behaviors for Mg-doped In_2O_3. We believe that this method has a wide scope of application for the preparation of monoliths of complex metal oxides of macroporous type from suitable layered double hydroxides as the precursors.

Introduction

Metal oxides of macroporous type are scientifically attractive in prevailing application fields, including catalysis, optoelectronics, separation, sorption, electrochemistry, and sensor technology,[1] because of their interesting electric, magnetic, and thermal properties or chemical resistance in harsh environments. At present, templating techniques using colloidal crystal,[1a,b,2] biopolymer gel,[3] synthetic polymer gel,[4] cellulose acetate membrane,[5] eggshell membrane,[6] and emulsion[7] as templates have been widely developed for the fabrication of such materials. Despite the drastic progress made in the template synthesis of the above metal oxide materials, it should be emphasized that most of the reported researches up to now are focused on simple metal oxides, and only few works concerning complex metal oxides are described.[8] Generally, complex metal oxides can exhibit unique chemical and physical properties due to their variable compositions and find important applications in various areas. In addition, monolith type of complex metal oxides can further facilitate practical applications compared with powders or fragile films types. Therefore, a lot of benefits would be obtained if complex metal oxide monoliths of macroporous type could be synthesized.

The selective leaching (dissolution) method has a long history and is established to be a versatile synthesis approach for various porous materials on a wide length scale (from nanometers to micrometers), in which at least two phases of different solubility should exist at leaching conditions. For example, Raney nickel catalyst can be obtained by leaching

---

* To whom all correspondence should be addressed: Tel 8610-64451226, Fax 8610-64425385, e-mail lifeng_70@163.com.

(1) (a) Blanford, C. F.; Yan, H.; Schroden, R. C.; Al-Daous, M.; Stein, A. *Adv. Mater.* **2001**, *13*, 401. (b) Stein, A.; Schroden, R. C. *Curr. Opin. Solid State Mater. Sci.* **2001**, *5*, 553. (c) Carreon, M. A.; Guliants, V. V. *Eur. J. Inorg. Chem.* **2005**, 27.

(2) (a) Holland, B. T.; Blanford, C. F.; Stein, A. *Science* **1998**, *281*, 538. (b) Soten, I.; Miguez, H.; Yang, S. M.; Perrov, S.; Coombs, N.; Tetreault, N.; Matsuura, N.; Ruda, H. E.; Ozin, G. A. *Adv. Funct. Mater.* **2002**, *18*, 71. (c) Fu, M.; Zhou, J.; Xiao, Q.; Li, B.; Zong, R.; Chen, W.; Zhang, J. *Adv. Mater.* **2006**, *18*, 1001.

(3) (a) Walsh, D.; Arcelli, L.; Ikoma, T.; Tanaka, J.; Mann, S. *Nat. Mater.* **2003**, *2*, 386. (b) Zhang, B.; Davis, M. A.; Mann, S. *Chem. Mater.* **2002**, *14*, 1369.

(4) (a) Schattka, J. H.; Shchukin, D. G.; Jia, J.; Antonietti, M.; Caruso, R. A. *Chem. Mater.* **2002**, *14*, 5103. (b) Shchukin, D. G.; Yaremchenko, A. A.; Ferreira, M. G. S.; Kharton, V. V. *Chem. Mater.* **2005**, *17*, 5124.

(5) (a) Caruso, R. A.; Schattka, J. H. *Adv. Mater.* **2000**, *12*, 1921. (b) Shchukin, D. G.; Caruso, R. A. *Adv. Funct. Mater.* **2003**, *13*, 789. (c) Wang, Y.; Tang, Y.; Dong, A.; Wang, X.; Ren, N.; Shan, W.; Gao, Z. *Adv. Mater.* **2002**, *14*, 994.

(6) (a) Yang, D.; Qi, L.; Ma, J. *Adv. Mater.* **2002**, *14*, 1543. (b) Yang, D.; Qi, L.; Ma, J. *J. Mater. Chem.* **2003**, *13*, 1119.

(7) (a) Imhot, A.; Pine, D. J. *Nature (London)* **1997**, *389*, 948. (b) Zhang, H.; Hardy, G. C.; Khimyak, Y. Z.; Rosseinsky, M. J.; Cooper, A. J. *Chem. Mater.* **2004**, *16*, 4245.

(8) (a) Soten, I.; Miguez, H.; Yang, S. M.; Petrov, S.; Coombs, N.; Tetreault, N.; Matsuura, N.; Ruda, H. E.; Ozin, G. A. *Adv. Funct. Mater.* **2002**, *12*, 71. (b) Sadakane, M.; Asanuma, T.; Kubo, J.; Ueda, W. *Chem. Mater.* **2005**, *17*, 3546. (c) Toberer, E. S.; Seshadri, R. *Adv. Mater.* **2005**, *17*, 2244. (d) Sokolov, S.; Stein, A. *Mater. Lett.* **2003**, *57*, 3593. (e) Chi, E. O.; Kim, Y. C.; Hur, N. H. *Chem. Mater.* **2003**, *15*, 1929.

10.1021/cm702309e CCC: \$37.00

aluminum (silicon) phase out of a Ni–Al (Ni–Si) alloy with an alkali solution.[9] Similarly, this technique has also been reported for the fabrication of nanoporous gold,[10] macroporous YSZ (Y_2O_3-stabilized ZrO_2),[11] porous silica,[12] glasses,[13] ceramics,[14] and so on. Recently, Seshadri and co-workers also extended this technique to fabricate macroporous monoliths of inorganic materials including complex oxides and metals with the combination of the vapor-phase leaching method.[8c,15]

Layered double hydroxides (LDHs), also known as hydrotalcite-like materials, are a class of synthetic anionic clays, in which the metal ions are bonded to hydroxyl groups to form two-dimensional brucite-like layers that are stacked together through electrostatic interactions between interlayer anions and positively charged layers.[16] Within the layers, the cations are *uniformly distributed on an atomic level* without segregation of "lakes" of separate cations.[17] Calcination of LDHs is known to give spinels, but these are always mixed with the oxide of the divalent metal.[16] This reflects the fact that in LDHs the ratio M^{II}/M^{III} is typically[16] in the range 2–4, whereas in a spinel the required ratio is $M^{II}/M^{III} = 0.5$. Recently, we developed a series of novel routes to obtain pure spinel-type complex metal oxides through LDH precursors.[18] One approach is that zinc aluminate spinels ($ZnAl_2O_4$) with mesopore networks and unusually high specific surface areas could be prepared by selective leaching of ZnO sacrificial template self-generated during calcination of LDH precursor containing Zn^{2+} and Al^{3+} at 500 °C or above.[18c]

In this report, we describe a facile and flexible approach to fabricate a series of complex metal oxide monolith materials with macropore frameworks, including ceramic and catalytic $MgAl_2O_4$ spinels, magnetic $MgFe_2O_4$ ferrites, and transparent Mg-doped In_2O_3 ($In_{2-x}Mg_xO_3$) semiconductor materials, from a range of LDH precursors of the type $[Mg_{1-x}M^{3+}_x(OH)_2]^{x+}(CO_3^{2-})_{x/2}\cdot mH_2O$ (M = Al, Fe, and In). The synthetic strategy mainly involves the formation of a two-phase composite monolith containing the desired complex metal oxide and MgO, which is induced by high-temperature sintering of LDH precursors for a long time and subsequent phase separation by a selective leaching of self-generated MgO sacrificial template from the two-phase composite monolith. Figure 1 illustrates schematically the whole synthesis procedure, in which the phase formation and separation is the key factor, and no preintroducing templates are involved in the starting reactants. Meanwhile, the templating effect of formed MgO in the sintered precursors plays an important role in the accessible microstructures in resultant macroporous monoliths, especially morphologies, particle sizes, spacing among particles, and compositions, which can be finely tuned by varying the synthesis parameters such as sintering temperature and composition of LDH precursors. Furthermore, the interfacial, magnetic, and optical properties of as-prepared $MgAl_2O_4$, $MgFe_2O_4$, and $In_{2-x}Mg_xO_3$ monoliths with their tunable microstructures have been carefully investigated, respectively, which gives greater insight into the nature of Mg-containing complex metal oxide materials.

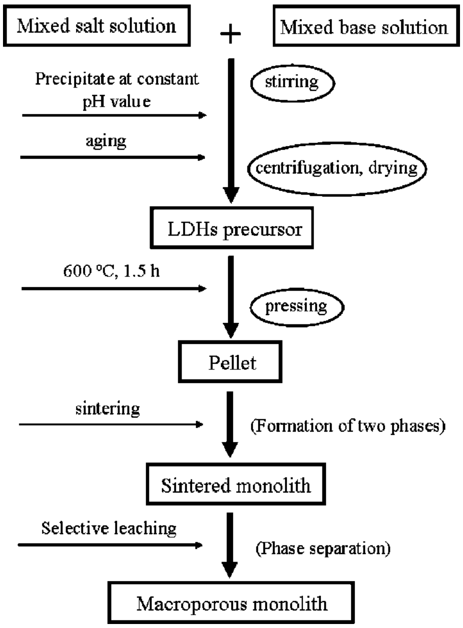

Figure 1. Schematic illustration of synthesis of macroporous complex metal oxide monoliths.

Experimental Section

Synthesis of Mg–M LDH Precursors (M = Al, Fe, and In). All the LDH samples were synthesized by a coprecipitation method in low supersaturation conditions at room temperature. After an aging step, the precipitates were separated by centrifugation and washed extensively with deionized water until pH 7–8. Afterward, the solids were dried at 60 °C for 24 h. A mixture of $Mg(NO_3)_2\cdot 6H_2O$ and $Fe(NO_3)_3\cdot 9H_2O$ with Mg^{2+}/Fe^{3+} molar ratio of 2.0, 3.0, and 4.0 was dissolved in 100 mL of deionized water to give solution A ($[Mg^{2+}] + [Fe^{3+}] = 1.2$ M). NaOH and Na_2CO_3 were dissolved in 100 mL of deionized water to give a mixed base solution B. The concentrations of the base were related to those of the metal ions in solution A as follows: $[CO_3^{2-}] = 2.0[Fe^{3+}]$, $[OH^-] = 1.6([Mg^{2+}] + [Fe^{3+}])$. Solutions A and B were simultaneously added dropwise to a four-necked flask containing 50 mL of deionized water at room temperature. The pH values for Mg–Fe

---

(9) Raney, M. U.S. Patent US1563787, 1925.

(10) Erlebacher, J.; Aziz, M. J.; Karma, A.; Dimitrov, N.; Sieradzki, K. *Science* **1998**, *281*, 538.

(11) (a) Gorte, R. J.; Vohs, J. M. *J. Catal.* **2003**, *216*, 477. (b) Kim, H.; Rosa, M. D.; Boaro, C.; Vohs, J.; Gorte, R. *J. Am. Ceram. Soc.* **1998**, *81*, 649.

(12) Okada, K.; Shimai, A.; Takei, T.; Hayashi, S.; Yasumori, A.; Mackenzie, K. J. D. *Microporous Mesoporous Mater.* **1998**, *21*, 289.

(13) Gille, W.; Enke, D.; Janowski, F.; Hahn, T. *J. Porous Mater.* **2003**, *10*, 179.

(14) Hosono, H.; Zhang, Z.; Abe, Y. *J. Am. Ceram. Soc.* **1989**, *72*, 1587.

(15) (a) Toberer, E. S.; Joshi, A.; Seshadri, R. *Chem. Mater.* **2005**, *17*, 2142. (b) Toberer, E. S.; Schladt, T. D.; Seshadri, R. *J. Am. Chem. Soc.* **2006**, *128*, 1462. (c) Toberer, E. S.; Löfvander, J. P.; Seshadri, R. *Chem. Mater.* **2006**, *18*, 1047. (d) Toberer, E. S.; Seshadri, R. *Chem. Commun.* **2006**, 3159.

(16) (a) Cavani, F.; Trifiró, F.; Vaccari, A. *Catal. Today* **1991**, *11*, 173. (b) Rives, V. *Layered Double Hydroxides: Present and Future*; Nova Sci. Pub.: New York, 2001. (c) Wypych, F.; Satyanarayana, K. G. *Clay Surface: Fundamentals and Applications*; Elsevier (Academic): London, 2004. (d) Evans, D. G.; Slade, R. C. T. *Struct. Bonding (Berlin)* **2006**, *119*, 1. (e) Li, F.; Duan, X. *Struct. Bonding (Berlin)* **2006**, *119*, 193.

(17) Vucelic, M.; Jones, W.; Moggridge, G. D. *Clays Clay Miner.* **1997**, *45*, 803.

(18) (a) Liu, J.; Li, F.; Evans, D. G.; Duan, X. *Chem. Commun* **2003**, 542. (b) Li, F.; Liu, J.; Evans, D. G.; Duan, X. *Chem. Mater.* **2004**, *16*, 1597. (c) Zou, L.; Li, F.; Xiang, X.; Evans, D. G; Duan, X. *Chem. Mater.* **2006**, *18*, 5852.

LDHs with different Mg^{2+}/Fe^{3+} molar ratio of 2.0, 3.0, and 4.0 were held constant at 9.0, 10.0, and 12.0, respectively. The resulting suspension was further aged at 80 °C for 10 h with stirring. The procedures for the preparation of Mg–Al and Mg–In LDHs are similar with that of Mg–Fe LDHs. The starting salts used here are $Al(NO_3)_3 \cdot 9H_2O$ and $In(NO_3)_3 \cdot 5H_2O$. The final pH values for both Mg–Al and Mg–In LDHs were held constant at 10.0.

Synthesis of Complex Metal Oxide Monoliths. The above Mg–M LDH precursors were calcined in air at 600 °C for 1.5 h. The obtained powder was ground by hand and then pressed into cylindrical pellets (13 mm diameter and ~1–2 mm high). Certainly, dimensions of the monolith could be adjusted according to the mold. After that, the pellets were sintered at high temperatures (1000–1200 °C) for 12 h. The sintered Mg–Al, Mg–Fe, and Mg–In LDH precursors are denoted S-NAl-T, S-NFe-T, and S-NIn-T, respectively, where N means the Mg^{2+}/M^{3+} molar ratio in the synthesis mixture and T means sintering temperature. Immersion of above sintered precursors in $(NH_4)_2SO_4$ solution (10 wt %, pH ≈ 6.0) at a temperature of 80 °C for 20 h (repeated twice) dissolved the MgO phase, leaving monoliths of $MgAl_2O_4$, $MgFe_2O_4$, and $In_{2-x}Mg_xO_3$, which were correspondingly denoted M-NAl-T, M-NFe-T, and M-NIn-T, respectively. Following the selective leaching, the pellets were washed in deionized water for 2 days with periodic replacement of water and dried at 60 °C for 12 h.

For comparison, the two dense complex metal oxide monoliths ($MgAl_2O_4$ and $MgFe_2O_4$) were prepared by pressing the powder obtained by the conventional ceramic method (1200 °C, 24 h for $MgAl_2O_4$; 1100 °C, 24 h for $MgFe_2O_4$) into cylindrical pellets (13 mm diameter and ~1–2 mm high).

Surface Modification of Monoliths. The surfaces of $MgAl_2O_4$ monoliths were subsequently modified by *n*-octadecanoic acid (C18 acid) self-assembled monolayers.[19] The $MgAl_2O_4$ monoliths were immersed into a 1 mM *n*-hexane solution of C18 acid at 30 °C for 4 days. Then they were rinsed by acetone and blown to dry with N_2 at room temperature.

Characterization. Powder X-ray diffraction (XRD) patterns of the samples were collected using a Shimadzu XRD-6000 diffractometer under the following conditions: 40 kV, 30 mA, graphite-filtered Cu Kα radiation ($\lambda = 0.154\,18$ nm). The samples, as unoriented powders, were step-scanned in steps of 0.04° (2θ) using a count time of 10 s/step. The observed diffraction peaks were corrected using elemental Si as an internal standard [$d(111) = 0.313\,55$ nm; JCPDS no. 27-1402]. The samples were grinded into powder before measurements.

Room temperature Fourier transform infrared (FT-IR) spectra were recorded in the range 4000–400 cm^{-1} with 2 cm^{-1} resolution on a Bruker Vector-22 Fourier transform spectrometer using the KBr pellet technique (1 mg of sample in 100 mg of KBr). FT-IR spectra of $MgAl_2O_4$ monoliths were recorded in the attenuated total reflection mode (ATR-FTIR) over a wavenumber range from 650 to 4000 cm^{-1}.

Thermogravimetric and differential thermal analysis (TG-DTA) were carried out in air on a HCT-2 thermal analysis system produced locally. Samples of 10.0 mg were heated at a rate of 10 °C/min up to 1100 °C.

Hitachi S-3500N and S-4700 scanning electron microscopes (SEM) and an Oxford Instrument Isis300 energy dispersive X-ray spectrometer (EDX) were employed to observe the morphology and analyze chemical composition. The accelerating voltage was 20 kV.

N_2 sorption measurements were performed at 77 K using a Quantachrome Autosorb-1C-VP system. Prior to the measurements, samples were degassed at 200 °C for 3 h.

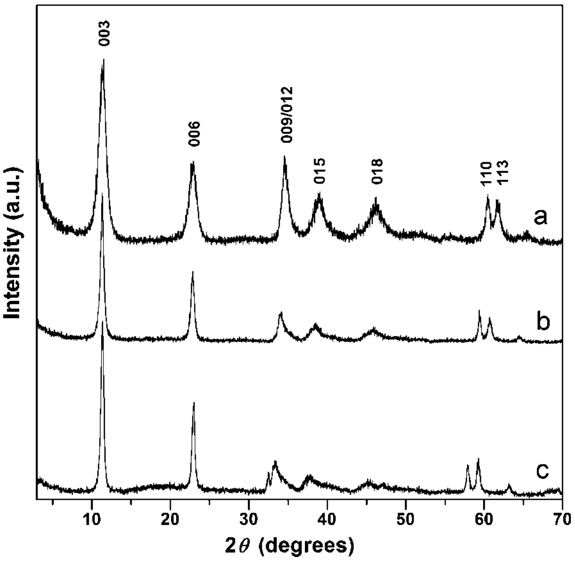

Figure 2. Powder XRD patterns of (a) Mg–Al LDH, (b) Mg–Fe LDH, and (c) Mg–In LDH.

Water contact angles (CAs) were measured with a sessile drop (5 μL) at three different points of each sample using a commercial drop-shape analysis system (DSA100, KRüSS GmbH, Germany) at ambient temperature.

Magnetism of samples at room temperature was measured using a LDJ9600 vibrating sample magnetometer of 5×10^{-6} emu sensitivity. Temperature and field dependences of the magnetization of monoliths were measured on a Quantum Design MPMS-XL SQUID operating in the temperature range 5–400 K.

Solid state UV–vis diffuse reflectance spectra (DRS) were recorded at room temperature and in air by means of a Shimadzu UV-2501PC spectrometer equipped with an integrating sphere attachment using $BaSO_4$ as background.

The photoluminescence (PL) measurement was carried out by using a Shimadzu RF PC-5301 spectrofluorophotometer at room temperature. A 150 W xenon lamp was used as the excitation source.

Results and Discussion

Synthesis and Characterization of Mg–M LDH Precursors (M = Al, Fe, and In). Figure 2 shows the powder XRD patterns of Mg–M LDHs (M = Al, Fe, and In) with Mg/M molar ratio of 3:1. It is obviously seen that three samples display only the characteristic X-ray diffraction peaks corresponding to hydrotalcite-like LDH family, i.e., (003), (006), (009), (110), and (113),[20,21] while the intensive and sharp diffraction peaks reveal the highly crystalline nature and excellent layered feature of the samples. Assuming a 3R stacking of the layers, the lattice parameters *a* represents the mean cation–cation distance within the brucite-like layer ($=2d_{110}$). Correspondingly, the calculated lattice parameter *a* increases gradually from Mg–Al LDH (3.061 Å) to Mg–Fe LDH (3.111 Å) and Mg–In LDH (3.184 Å), reflecting the fact that the ionic radii for Al^{3+}, Fe^{3+}, and In^{3+} are 0.50, 0.64, and 0.81 Å, respectively.

---

[19] Wu, X.; Zhang, L.; Wu, D. *Langmuir* **2005**, *21*, 2665.

[20] Busetto, C.; Del Piero, G.; Mamara, G.; Trifiró, F.; Vaccari, A. *J. Catal.* **1984**, *85*, 260.

[21] Millange, F.; Walton, R. I.; O'Hare, D. *J. Mater. Chem.* **2000**, *10*, 1713.

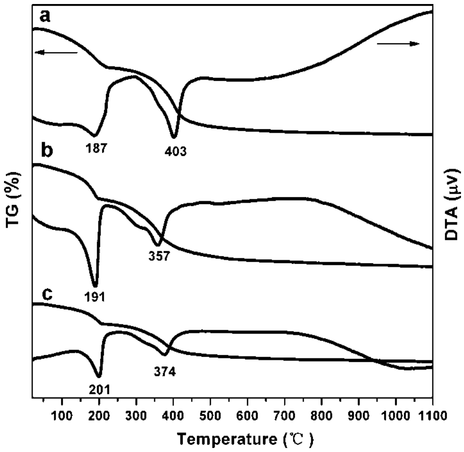

Figure 3. TG-DTA curves of (a) Mg–Al, (b) Mg–Fe, and (c) Mg–In LDH precursors.

The FT-IR spectra of three LDH samples in the region 400–4000 cm^{-1} (Figure S1 in Supporting Information) show typical absorption peaks of hydrotalcite-like phase with CO_3^{2-} as counteranion.[22] The strong and broad absorption band observed around 3600–3200 cm^{-1} is associated with a superposition of the hydroxyl stretching band $\nu(OH_{str})$ arising from metal–hydroxyl groups and hydrogen-bonded interlayer water molecules. Another absorption band corresponding to water deformation, $\delta(H_2O)$, is recorded around 1635 cm^{-1}. An intense absorption band between 1358 and 1384 cm^{-1} is ascribed to the ν_3 (asymmetric stretching) mode of the CO_3^{2-} ions in the interlayer. The blue shift of this band compared to that observed for the free carbonate anion (ca. 1415 cm^{-1}) is attributed to the restrictions imposed by the interlayer gallery. The other bands observed in the low-frequency 500–800 cm^{-1} region are interpreted as the vibration modes of metal–oxygen (M–O) and metal–hydroxyl (M–OH) groups in the lattices.[23]

Generally, the thermal stability of LDH materials depends on several factors such as the nature of cations, cationic compositions, the nature of interlayer anions, the crystallinity of materials, etc.[24] Note from the TG-DTA profiles of LDHs (Figure 3) that in each case the weight loss occurs essentially in two steps.[16a] The first one in the temperature range from room temperature up to ca. 220 °C corresponds to removal of water physisorbed on the external surface of the crystallites as well as water intercalated in the interlayer galleries, which correspondingly is related to an endothermic event in the DTA at around 180–210 °C. The second weight loss involves dehydroxylation of the layers and loss of volatile species arising from decomposition of the interlayer carbonate anions. This process is accompanied by an endothermic event in the DTA between 350 and 410 °C. Furthermore, it is observed that there is no notable weight loss in the TG curves at above 600 °C. As a result, the LDH precursors were first calcined at 600 °C before the sintering process to avoid the fragmentation of the resultant monoliths.

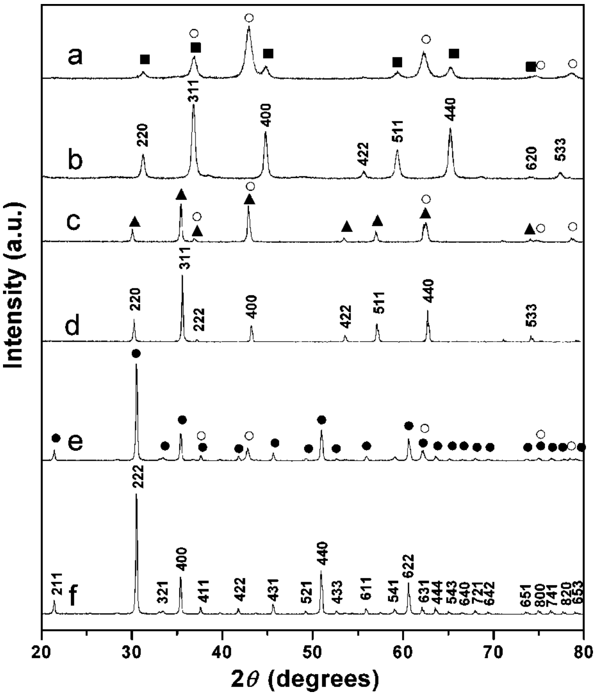

Figure 4. Powder XRD patterns of sintered precursors with Mg/M^{3+} molar ratio of 3.0 at 1000 °C (a) sintered MgAl-LDH (S-3Al-1000), (c) sintered MgFe-LDH (S-3Fe-1000), and (e) sintered MgIn-LDH (S-3In-1000) and resultant monoliths (b) $MgAl_2O_4$ (M-3Al-1000), (d) $MgFe_2O_4$ (M-3Fe-1000), and (f) $In_{2-x}Mg_xO_3$ (M-3In-1000) after selective leaching of MgO. (■) $MgAl_2O_4$; (▲) $MgFe_2O_4$; (●) In_2O_3; (○) MgO.

Synthesis of Complex Metal Oxide Monoliths. Figure 4 shows the power XRD patterns of sintered Mg–M LDHs (M = Al, Fe, and In) with Mg/M molar ratio of 3:1 at 1000 °C (S-3Al-1000, S-3Fe-1000, and S-3In-1000) and resultant monoliths (M-3Al-1000, M-3Fe-1000, and M-3In-1000). It is observed that two-phase composites (complex metal oxide and MgO phases) have been obtained after the sintering process, and selective leaching with 10 wt % $(NH_4)_2SO_4$ aqueous solution completely removes the MgO (periclase) phase, leading to the formation of pristine complex metal oxide monoliths. To take the preparation of S-3Al-1000 as an example, X-ray characteristic diffraction peaks of MgO and cubic $MgAl_2O_4$ spinel phases appear simultaneously in S-3Al-1000. After selective leaching, MgO phase is completely removed and only the $MgAl_2O_4$ phase (JCPDS 21-1152) remains. Also, the partial superposition of X-ray diffraction peaks of MgO and $MgFe_2O_4$ spinel in S-3Fe-1000 is observed, due to the fact that the lattice parameter *a* of $MgFe_2O_4$ spinel (a = 8.397 Å, JCPDS 17-0465) is about 2 times that of cubic MgO structure (a = 4.211 Å, JCPDS 45-0946). It is worthy to note that the obtained spinel seems to be much more crystallized after the selective leaching than before. This should be assigned to the segregation effect of MgO, resulting in the existence of a large number of "isolated" spinel particles with MgO in sintered precursors and thus much wider half-width of diffraction lines than those in the resultant monoliths without MgO. Unlike M-3Al-1000 and M-3Fe-1000, spinel-type complex metal oxide ($MgIn_2O_4$) has not been found in M-3In-1000, and only the In_2O_3 phase

---

(22) Hernandez-Moreno, M. J.; Ulibarri, M. A.; Rendon, J. L. *Phys. Chem. Miner.* **1985**, *12*, 34.

(23) Titulaer, M. K.; Jansen, J. B. H.; Geus, J. W. *Clays Clay Miner.* **1994**, *42*, 249.

(24) Braterman, P. S.; Xu, Z. P.; Yarberry, F. *Handbook of Layered Materials*; Marcel Dekker: New York, 2004; Chapter 8, pp 373–474.

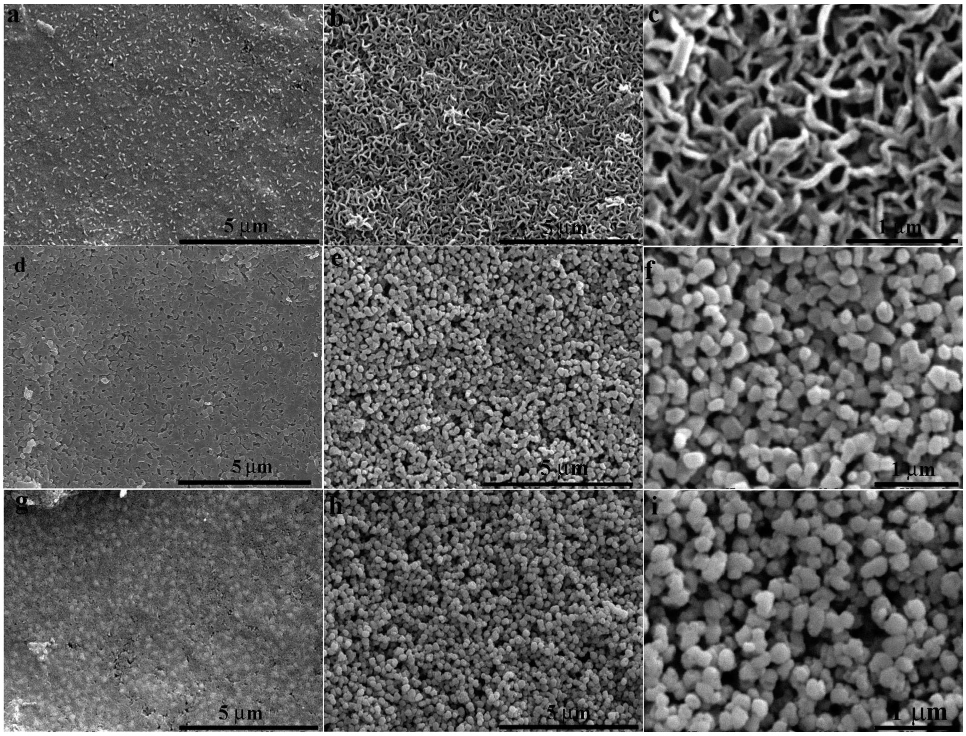

Figure 5. Typical SEM images of sintered precursors with Mg/M^{3+} molar ratio of 3.0 at 1000 °C (a) sintered MgAl-LDH (S-3Al-1000), (d) sintered MgFe-LDH (S-3Fe-1000), and (g) sintered MgIn-LDH (S-3In-1000) and resultant monoliths after selective leaching of MgO (b, c) $MgAl_2O_4$ (M-3Al-1000), (e, f) $MgFe_2O_4$ (M-3Fe-1000), and (h, i) $In_{2-x}Mg_xO_3$ (M-3In-1000).

is observed. This is because the formation of $MgIn_2O_4$ usually requires higher transform temperature of above 1300 °C.[25] However, the EDX result (Figure S2 in Supporting Information) shows that the Mg/(Mg + In) molar ratio in M-3In-1000 is around 9%, while element mapping exhibits homogeneous distributions of element Mg and In. In addition, it is found that the calculated lattice parameter a of M-3In-1000 is 10.12 Å, which is very close to the literature value of In_2O_3 ($a = 10.11$ Å, JCPDS 71-2195). As a result, it may be deduced that during the high-temperature treatment In^{3+} ions in the In_2O_3 lattices have been partially replaced by Mg^{2+} ions due to close ionic radius (0.081 nm for In^{3+} and 0.080 nm for Mg^{2+}), leading to the formation of Mg-doped In_2O_3 ($In_{1.82}Mg_{0.18}O_3$) solid solution.

The morphologies of monoliths were characterized by SEM (Figure 5). It is noted that although all sintered precursors show the dense surface with almost no porosity as a common characteristic (Figure 5a,d,g), three complex metal oxides monoliths (M-3Al-1000, M-3Fe-1000, and M-3In-1000) with different characterization of morphology are obtained after removal of MgO phase. For M-3Al-1000, curved and slim $MgAl_2O_4$ spinel crystals seem to connect with each other and form a well-developed three-dimensional netlike structure (Figure 5b,c), which should be facile for fluid transport in catalysis systems. For M-3Fe-1000, it is noted from Figure 5e that the morphology of $MgFe_2O_4$ monoliths exhibits aggregation of roughly spherical particles in the micrometer range. This kind of similar morphology is also observed for the M-3In-1000 sample. The difference in morphologies between M-3Fe-1000 (or M-3In-1000) and M-3Al-1000 comes from the different sintering behaviors of precursors. Besides, further N_2 sorption characterization (Figure S3 in Supporting Information) reveals that obvious mesoporous structure is absent in the complex metal oxides monoliths, except M-3Al-1000 sample. The M-3Al-1000 exhibits a BJH pore size distribution (around 2–30 nm) with a maximum at ~10 nm. The existence of mesopores should be related to the unique three-dimensional netlike structure in the sample.

Microstructural Control of Complex Metal Oxide Monoliths. A wide range of microstructures (morphologies, particle sizes, spacing among particles, and compositions) of $MgAl_2O_4$, $MgFe_2O_4$, and $In_{2-x}Mg_xO_3$ monoliths are achieved by adjusting the synthesis parameters such as sintering temperature and composition of precursors, which can control the formation process of the two-phase composite.

Figure 6 shows the XRD patterns and SEM images of sintered precursors and resultant monoliths at higher sintering temperature of 1100 °C (S-3Al-1100 and M-3Al-1100). The XRD patterns of samples reveal that pure $MgAl_2O_4$ phase is also obtained after complete removal of MgO phase. Note that S-3Al-1100 sample is nonporous in the micrometer range, while unlike M-3Al-1000, a macropore framework with closely interconnected $MgAl_2O_4$ particles is characteristic of resultant M-3Al-1100.

To tailor the microstructures of $MgFe_2O_4$ monoliths, the starting Mg–Fe LDH precursors with different Mg/Fe molar ratios of 2 and 4 were used. XRD results (not shown) confirmed the successful formation of two monoliths. A close look at SEM images (Figure 7) also reveals the existence of macropore frameworks with closely interconnected particles in M-2Fe-1000 and M-4Fe-100 monoliths. According to

---

(25) Dali, S. E.; Jayachamdran, M.; Chockalingam, M. J. *J. Mater. Sci. Lett.* **1999**, *18*, 915.

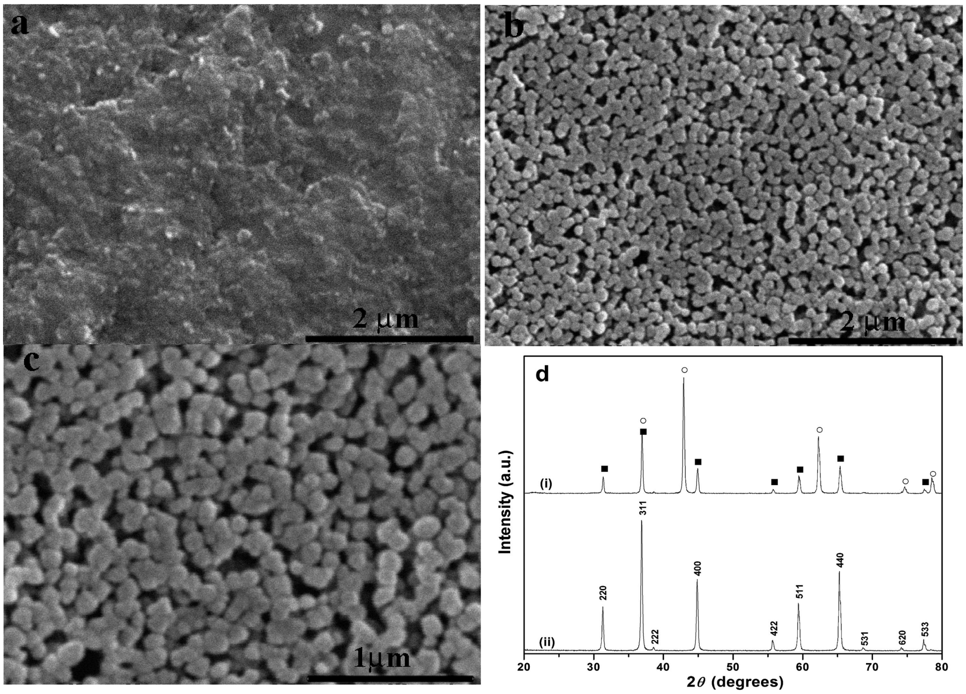

Figure 6. Typical SEM images of sintered precursor with Mg/Al molar ratio of 3.0 at 1100 °C (a) sintered MgAl-LDH (S-3Al-1100), (b) resultant $MgAl_2O_4$ monolith after selective leaching of MgO (M-3Al-1100), (c) a high-magnification SEM image of $MgAl_2O_4$ monolith, and (d) XRD pattern of (i) sintered MgAl-LDH and (ii) resultant $MgAl_2O_4$ monolith. (■) $MgAl_2O_4$; (○) MgO.

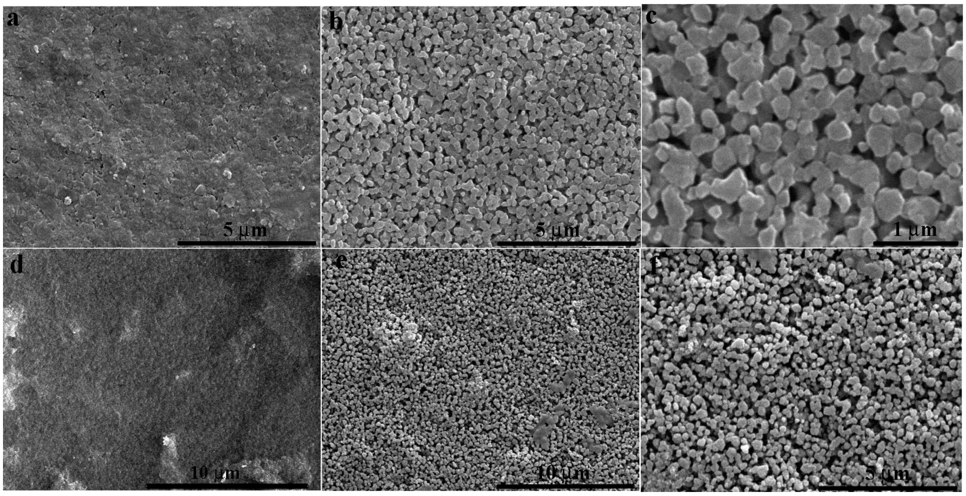

Figure 7. Typical SEM images of sintered precursors at 1000 °C (a) sintered MgFe-LDH with Mg/Fe molar ratio of 2.0 (S-2Fe-1000) and (d) sintered MgFe-LDH with Mg/Fe molar ratio of 4.0 (S-4Fe-1000), and resultant $MgFe_2O_4$ monoliths after selective leaching of MgO (b, c) M-2Fe-1000 and (e, f) M-4Fe-1000.

SEM images, the estimated $MgFe_2O_4$ particle sizes are about 0.32, 0.20, and 0.18 μm for M-2Fe-1000, M-3Fe-1000, and M-4Fe-1000 samples, respectively, decreasing with the content of Mg in precursors. Besides, in our case, it is difficult to determine and compare the macropore parameters of three $MgFe_2O_4$ monoliths through the mercury porosimetry measurement due to the great difference and complexity in the pore shape of samples. The system of $MgAl_2O_4$ monoliths also is in the way. However, it is noted from SEM images that the spacing among particles for $MgFe_2O_4$ monoliths increases gradually with the content of Mg in the precursors. Therefore, one can conclude that the higher the Mg content in precursors, the smaller the particle size and the larger the spacing among particles for $MgFe_2O_4$ monoliths. The kind of tuning mechanism for the microstructure of monoliths by adjusting the composition of precursors is proposed as follows:

$$Mg_nFe(OH)_{2n+2}(CO_3)_{0.5}{\cdot}mH_2O \rightarrow (n-0.5)MgO + 0.5MgFe_2O_4 + 0.5CO_2 + (n+m+1)H_2O \quad (n = 2, 3, \text{or } 4) \tag{1}$$

During the sintering process of precursors, both MgO and $MgFe_2O_4$ phases begin to form. It can be calculated from eq 1 that the $MgO/MgFe_2O_4$ molar ratio in S-2Fe-1000, S-3Fe-1000, and S-4Fe-1000 is 3, 5, and 7, respectively. As a result, the spacing among particles of resultant $MgFe_2O_4$ monolith increases progressively with the content of Mg in the precursors due to leaching of the increasing amount of

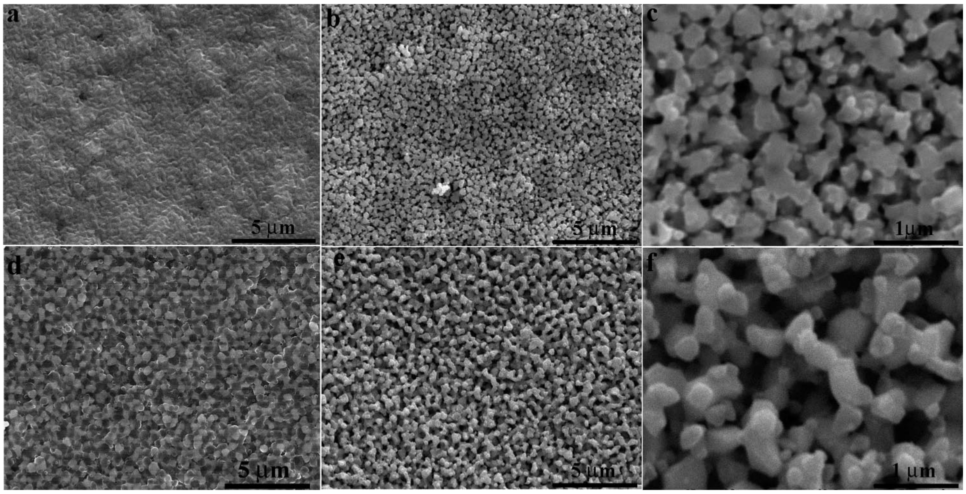

Figure 8. Typical SEM images of sintered precursors with Mg/In molar ratio of 3.0 (a) sintered MgIn-LDH at 1100 °C (S-3In-1100) and (d) sintered MgIn-LDH at 1200 °C (S-3In-1200) and resultant $In_{2-x}Mg_xO_3$ monoliths after selective leaching of MgO (b, c) M-3In-1100 and (e, f) M-3In-1200.

MgO. On the other hand, considering that the particle growth is controlled by the boundaries between particles,[26] one can assume that the mean boundary velocity, ν, is proportional to the thermodynamic driving force, ΔF, applied to eq 2

$$\nu = M\Delta F \tag{2}$$

where kinetic parameter M is the particle-boundary mobility, which depends on the diffusion mechanism. Therefore, two different approaches including reduction of M and ΔF can be used to prevent particle growth. In our system of sintered Mg–Fe LDHs, large amounts of MgO around target $MgFe_2O_4$ particles will obviously reduce the particle-boundary mobility during the sintering process, and this effect becomes more and more remarkable with the amount of MgO. Meanwhile, the decrease of ΔF also exists when large amounts of MgO are around $MgFe_2O_4$ particles but is independent of the amount of MgO. Such decrease in ΔF has already been confirmed by experimental and theoretical evidence in metal solid solution system.[27] Hence, larger amounts of MgO sacrificial phase also have a more remarkable segregation and inhibition effect on the growth of $MgFe_2O_4$ spinel, leading to decreasing particle size in $MgFe_2O_4$ monoliths with Mg content in the precursors. Besides, note that the decreasing trend in particle size of $MgFe_2O_4$ from M-3Fe-1000 to M-4Fe-1000 is not very obvious. This is because in S-3Fe-1000 5 times the amount of MgO sacrificial phase than that of $MgFe_2O_4$ has already exhibited enough segregation and inhibition effect on the growth of $MgFe_2O_4$.

In the $In_{2-x}Mg_xO_3$ system, higher sintering temperatures (1100 and 1200 °C) were adopted to control the microstructure of monolith. XRD results (Figure S4 in Supporting Information) also reveal that two $In_{2-x}Mg_xO_3$ monoliths have been obtained successfully at higher sintering temperatures. One can particularly observe apparent difference in the microstructures of $In_{2-x}Mg_xO_3$ monoliths (Figure 8). With the sintering temperature, resultant $In_{2-x}Mg_xO_3$ monoliths exhibit more prominent macropore framework with the larger spacing among interconnected particles due to the increasing degree of particles' sintering. EDX spectroscopy also gives out the formula of $In_{1.80}Mg_{0.20}O_3$ for M-3In-1100 and $In_{1.74}Mg_{0.26}O_3$ for M-3In-1200, the lattice parameters a of which are 10.12 and 10.13 Å determined by XRD patterns. This indicates that the sintering at higher temperature would facilitate more Mg^{2+} ions into the In_2O_3 lattices, resulting in the increase of lattice parameter a.

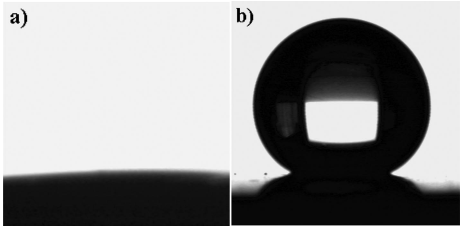

Figure 9. Shape of a water droplet on the surface of $MgAl_2O_4$ monoliths: (a) unmodified and (b) *n*-octadecanoic acid-modified M-3Al-1100.

Properties of Complex Metal Oxide Monoliths. As the efficacy of materials depends on their microstructures, which can play a very important role with regard to the chemical and physical properties of materials, the interfacial, magnetic, and optical properties of as-prepared Mg-containing complex metal oxide monolith materials, $MgAl_2O_4$, $MgFe_2O_4$, and $In_{2-x}Mg_xO_3$, are preliminarily delineated, respectively.

$MgAl_2O_4$ spinel is an important ceramic material with high melting temperature (2135 °C) and good chemical stability and mechanical strength.[28] It is observed in Figure 9a that when a water droplet is dripped onto $MgAl_2O_4$ monolith (M-3Al-1100), it spreads very quickly onto the surface with low water contact angle (CA) of about 8°, indicating the surface superhydrophilicity of this monolith due to "high-energy interfaces" for metal oxide surfaces. If the surface of above $MgAl_2O_4$ monoliths could be endowed with surface hydrophobicity, they would be promising engineering materials for wide applications. To achieve the surface hydrophobicity, the M-3Al-1100 sample was modified by *n*-octadecanoic acid (C18 acid) self-assembled monolayer. The ATR-FTIR spec-

---

(26) Chiang, Y. M.; Birnie III, D. P.; Kingery, W. D. *Physical Ceramic-Principles for Ceramic Science and Engineering*; John Wiley and Sons: New York, 1997.

(27) Gleiter, H. *Acta Mater.* **2000**, *48*, 1.

(28) (a) Wu, X. C.; Tao, Y. R.; Han, Z. J.; Zhang, B. D. *J. Mater. Chem* **2003**, *13*, 2649. (b) Guo, J.; Lou, H.; Zhao, H.; Wang, X.; Zheng, X. *Mater. Lett.* **2004**, *58*, 1920.

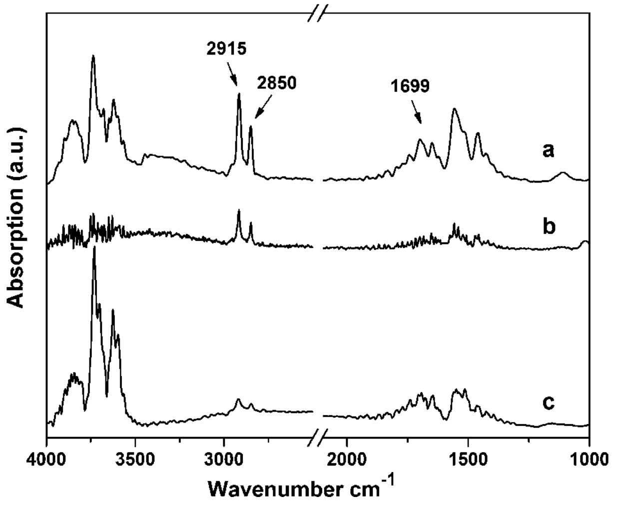

Figure 10. ATR-FTIR spectra of modified $MgAl_2O_4$ monolith (a) M-3Al-1000, (b) M-3Al-1100, and (c) modified dense $MgAl_2O_4$ monolith.

trum of modified $MgAl_2O_4$ monoliths (Figure 10) shows that two strong peaks at 2850 cm^{-1} (ν_{CH_2}) and 2915 cm^{-1} (ν_{CH_3}) are observed, as a result of the existence of the long-chain aliphatic groups on the surface. The peak at 1699 cm^{-1} is ascribed to carbonyl stretching band ($\nu_{C=O}$). The results reflect that the surface of $MgAl_2O_4$ monolith was successfully self-assembled by a monolayer of hydrophobic long-chain C18 acid through the hydrogen bond interaction between carboxyl groups and surface oxygens of monolith. Correspondingly, the nonpolar tails of C18 acid self-assembled monolayer should be exposed to air. Figure 9b shows an image of water droplet on modified M-3Al-1100 sample, the water CA of which is found to be about 152 ± 2°, indicative of excellent surface superhydrophobicity. To the best of our knowledge, no one has reported the surface superhydrophobicity based on spinel-type ceramic materials. Besides, the enhanced surface hydrophobicity of modified M-3Al-1000 sample with the water CA of about 155 ± 2° (not shown) has been achieved. This is mainly because of the existence of more surface oxygens on the $MgAl_2O_4$ monolith upon sintering at lower temperature, as confirmed by ATR-FTIR results (Figure 10), that is, the higher amount of C18 acid on the surface of modified M-3Al-1000 sample. In a way, the small difference in surface hydrophobicity between two samples is also related to different surface morphology. However, such surface superhydrophobic property has not been found in the modified dense $MgAl_2O_4$ monolith by C18 acid (the measured CA is 102 ± 2°) due to the deficiency of rough microstructure on the dense surface[29] as well less surface oxygens on the monolith (Figure 10c).

The temperature dependence of magnetization for $MgFe_2O_4$ monoliths was investigated by a superconducting quantum interference device (SQUID) magnetometer (Figure 11a). It is observed that the zero field cooled (ZFC) magnetization increases continuously from 5 to 400 K, whereas its field cooled (FC) magnetization decreases gradually with the temperature and at last overlaps with the ZFC results. Such absence of the Verwey transition signature has also been observed in the recent reported mesoporous Fe_3O_4 and γ-Fe_2O_3[30] and some other cases,[31] though the actual reason has not been explained. In our system, it should be related to the existence of unique porous structure and large $MgFe_2O_4$ ferrite particles in the monoliths. Besides, all the ZFC and FC curves of three monoliths exhibit similar behaviors except a step in the ZFC curve for M-3Fe-1000 sample from about 150 to 300 K. This step is considered to be a spin (cluster) transition, which has been seen in nanocrystalline ferrites because of the frozen canted spins in the grain surface region.[32]

The field dependence of magnetization for $MgFe_2O_4$ monoliths was also measured using a vibrating sample magnetometer (VSM) at room temperature. The hysteresis loops are shown in Figure 11b. Clearly, the measured saturation magnetization depends on the microstructures and increases progressively from 25.4 for M-2Fe-1000 to 39.5 for M-3Fe-1000 and 42.7 emu/g for M-4Fe-1000. In previous studies, the saturation magnetization for $MgFe_2O_4$ powders usually varies between 18 and 30 emu/g depending on the synthesis technique employed[33] (26.4 emu/g for $MgFe_2O_4$ spinel by conventional ceramic method[18b]). The enhanced saturation magnetization for $MgFe_2O_4$ monoliths may originate from as follows. LDHs possess several advantages as a single-source precursor to spinel ferrite that lead to enhance saturation magnetization. Use of a molecular precursor with cations randomly distributed with no long order facilitates the synthesis of homogeneous spinel phase.[16a] The close structural relationship between the LDH precursor and its corresponding spinel product (the 110 diffraction of LDH transforms to 440 spinel diffraction) is another key factor.[34] Such enhancement of saturation magnetization has been confirmed in our recent studies on a series of spinel ferrite powders synthesized from tailored LDHs precursors.[18a,b] On the other hand, it should be noted that the well-documented rule for the size-dependent superparamagnetic properties of $MgFe_2O_4$ nanocrystallites[35] (the saturation magnetization enlarges continuously with the particle size from 6 to 13 nm) is not suitable here. This is because the superparamagnetic properties no longer exist in monoliths due to larger particle sizes in the range of micrometer. Besides, the quite

---

(29) (a) Fu, Q.; Rama Rao, G. V.; Basame, S. B.; Keller, D. J.; Artyushkova, K.; Fulghum, J. E.; López, G. P. *J. Am. Chem. Soc.* **2004**, *126*, 8904. (b) Feng, L.; Li, S.; Li, Y.; Li, H.; Zhang, L.; Zhai, J.; Song, Y.; Liu, B.; Jiang, L.; Zhu, D. *Adv. Mater.* **2002**, *14*, 1857. (c) Shang, H. M.; Wang, Y.; Limmer, S. J.; Chou, T. P.; Takahashi, K.; Cao, G. Z. *Thin Solid Films* **2005**, *472*, 37.

(30) Jiao, F.; Jumas, J.-C.; Womes, M.; Chadwick, A. V.; Harrison, A.; Bruce, P. G. *J. Am. Ceram. Soc.* **1989**, *72*, 1587.

(31) (a) Goya, G. F.; Berquo, T. S.; Fonseca, F. C.; Morales, M. P. *J. Appl. Phys.* **2003**, *94*, 3520. (b) Sena, S. P.; Lindley, R. A.; Blythe, H. J.; Sauer, C.; Al-Kafarji, M.; Gehring, G. A. *J. Magn. Magn. Mater.* **1997**, *176*, 111. (c) Chapline, M. G.; Wang, S. X. *J. Appl. Phys.* **2005**, *97*, 123901.

(32) (a) Oliver, S. A.; Handeh, H. H.; Ho, J. C. *Phys. Rev. B* **1999**, *60*, 3400. (b) Bhowmik, R. N.; Ranganathan, R.; Sarkar, S.; Bansal, C.; Nagarajan, R. *Phys. Rev. B* **2003**, *68*, 134433. (c) Stewart, S. J.; Mercader, R. C.; Vandenberghe, R. E.; Cernicchiaro, G.; Scorzelli, R. B. *J. Appl. Phys.* **2005**, *97*, 054304. (d) Kodama, R. H.; Berkowitz, A. E.; McNiff, E. J.; Foner, S. *J. Appl. Phys.* **1997**, *81*, 5552.

(33) Cross, W. B.; Affleck, L.; Kuznetsov, M. V.; Parlin, I. P.; Pankhurst, Q. A. *J. Mater. Chem.* **1999**, *9*, 2545.

(34) Bellotto, M.; Rebours, B.; Clause, O.; Lynch, J.; Bazin, D.; Elkaim, E. *J. Phys. Chem.* **1996**, *100*, 8535.

(35) (a) Chen, Q.; Zhang, Z. J. *Appl. Phys. Lett.* **1998**, *73*, 3156. (b) Liu, C.; Zou, B.; Rondinone, A. J.; Zhang, Z. J. *J. Am. Chem. Soc.* **2000**, *122*, 6263.

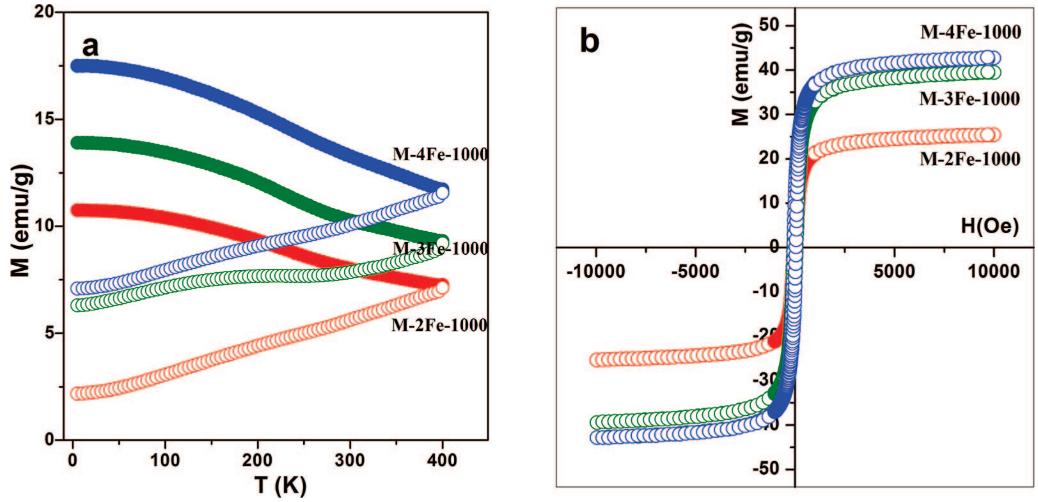

Figure 11. (a) Temperature dependence magnetization for $MgFe_2O_4$ monoliths in the ZFC and FC modes (the applied magnetic field is 100 Oe) and (b) magnetic hysteresis loops of $MgFe_2O_4$ monoliths at room temperature.

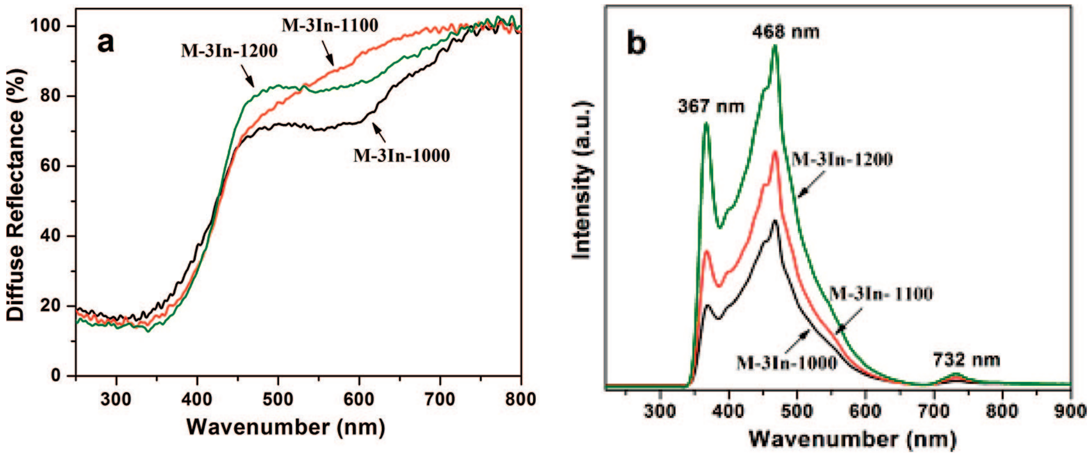

Figure 12. (a) UV–vis diffuse reflectance and (b) photoluminescence (PL) spectra of $In_{2-x}Mg_xO_3$ monoliths upon excitation at 290 nm at room temperature.

low coercivities for $MgFe_2O_4$ monoliths, which are 52, 64, and 56 Oe with the content of Mg in the precursors, should be ascribed to the low magnetocrystalline anisotropy of samples as a result of the absence of unpaired electrons in the Mg^{2+} cations of $MgFe_2O_4$ ferrite. However, the M-3Fe-1000 sample still exhibits the largest coercivity, which should be attributed to the spin canting, consistent with above ZFC result. The difference of saturation magnetization among three $MgFe_2O_4$ monoliths should comes from the different microstructures (particle sizes, spacing among the particles, and cation distributions).

In addition, the measured saturation magnetization for the dense $MgFe_2O_4$ monolith is about 22.0 emu/g, much lower than those of the above macroporous $MgFe_2O_4$ monoliths. This is probably because in the macroporous $MgFe_2O_4$ monoliths the interplay among the particles decreases due to existence of macroporous structure, which leads to the increase of interparticle exchange interaction and therefore the enhancement of saturation magnetization.[36]

In_2O_3 and related doped In_2O_3 are important transparent conducting oxides (TCOs) that are widely used as optoelectric devices, solar cells, sensors, flat panel displays, liquid crystal devices, etc.[37] Herein, for the first time, the optical properties of such monoliths materials are studied.

The UV–vis diffuse reflectance spectra of $In_{2-x}Mg_xO_3$ monoliths measured at room temperature are shown in Figure 12a. It can be found that the optical transmittances of three samples are relatively high in the visible region and much higher than that of ITO reported.[38] This high transparency, which is important for applications in many optical and electric devices, is expected in view of their macroporous structure. In addition, the so-called optical energy gap can be estimated using a classical Tauc approach.[39] It has been well-established that for a large number of semiconductors the dependence of the absorption coefficient α, for the high-frequency region, upon the photon energy E_p, for optically

---

(36) Zysler, R. D.; Fiorani, D.; Testa, A. M. *J. Magn. Magn. Mater.* **2001**, *224*, 5.

(37) (a) Zhang, D.; Liu, Z.; Li, C.; Tang, T.; Liu, X.; Han, S.; Lei, B.; Zhou, C. *Nano Lett.* **2004**, *4*, 1919. (b) Gopchandran, K. G.; Joseph, B.; Abraham, J. T.; Koshy, P.; Vaidyan, V. K. *Vacuum* **1997**, *48*, 547. (c) Zhang, D.; Li, C.; Liu, X.; Han, S.; Tang, T.; Zhou, C. *Appl. Phys. Lett.* **2003**, *83*, 1845. (d) Gordon, R. G. *MRS Bull.* **2000**, *25*, 52. (e) Shigesato, Y.; Takaki, S.; Haranoh, T. *J. Appl. Phys.* **1992**, *71*, 3356.

(38) Kawazoe, H.; Ueda, K. *J. Am. Ceram. Soc.* **1999**, *82*, 3330.

(39) Patil, P. S.; Kadam, L. D.; Lokhande, C. D. *Thin Solid Films* **1996**, *272*, 29.

induced transitions, is given by the following classical expression:[39]

$$\alpha E_p = K(E_p - E)^n \quad (3)$$

where E_g represents the optical band gap, E_p is the photon energy, K is a constant, and n depends on the nature of the transition. In our case of $In_{2-x}Mg_xO_3$ monoliths, the best fit of $(\alpha E_p)^2$ vs E_p was obtained for $n = {}^1/_2$ (Figure S5 in Supporting Information), suggesting the allowed direct transitions across the energy band gap of $In_{2-x}Mg_xO_3$ monoliths. This result is similar to that of reported Sn-doped In_2O_3 (ITO) films.[40] The extrapolated value (the straight lines to the x axis) of E_p at $\alpha = 0$ gives absorption edge energies corresponding to $E_g = 2.70$ for M-3In-1000, 2.72 for M-3In-1100, and 2.77 eV for M-3In-1200, which indicates that the optical band gaps of three $In_{2-x}Mg_xO_3$ monoliths are typical of wide band gap semiconductors. The small difference of E_g among three samples here comes from the different doped Mg content. Also, it is noted that the values of E_g for $In_{2-x}Mg_xO_3$ samples are smaller than those of pristine In_2O_3 (3.55–3.75 eV)[41] and ITO (3.5–4.3 eV),[40a,42] which should be ascribed to the change of crystal structure upon substituting Mg^{2+} ions for In^{3+} ions in In_2O_3 lattices.

Figure 12b shows the room temperature photoluminescence (PL) spectra of $In_{2-x}Mg_xO_3$ monoliths, which are excited at 290 nm using a Xe lamp at room temperature. It is seen that three samples exhibit nearly similar PL behaviors: strong ultraviolet emissions centered at 367 nm, intensively strong blue emissions centered at 468 nm, and weak emissions centered at 732 nm. It is known that the bulk In_2O_3 cannot emit light at room temperature.[43] Nevertheless, nanostructured In_2O_3 materials exhibit the blue luminescence emissions originating from the systematic oxygen vacancies, which has been well-documented in previous reports.[41,44] Herein, the blue emissions centered at 468 nm are also attributed to the existence of oxygen vacancies. This is because when the Mg ions (acceptors) replace In ions, oxygen vacancies (donors) are produced in In_2O_3 crystals by the self-compensation effect. These oxygen vacancies as deep defect donors in semiconductors would induce the formation of new energy levels in the band gap. Therefore, the radioactive recombination of a photoexcited hole with an electron occupying the oxygen vacancies results in the intensively strong blue emissions centered at 468 nm. In the case of UV emissions centered at 367 nm, one can first exclude the possibility of a quantum confinement effect because of the large particle size. The UV emission is due to the influence of the lattice defects existing in the Mg-doped In_2O_3. During the synthesis of $In_{2-x}Mg_xO_3$ monoliths, higher temperature sintering (above 1000 °C) is involved, and thus various kinds of defects such as indium vacancies or interstices, stacking faults, and so on may be introduced. The weak emissions centered at 732 nm is a result of the transition from the oxygen vacancies state to the O^{2-} state.[45] In addition, the measured PL intensity increases progressively from M-3In-1000 to M-3In-1100 and M-3In-1200, which is ascribed to the fact that the higher doped Mg content in $In_{2-x}Mg_xO_3$ monoliths, the higher concentration of oxygen vacancies and lattice defects.

Conclusions

In summary, we have successfully established a facile synthesis approach to complex metal oxides ($MgAl_2O_4$, $MgFe_2O_4$, and $In_{2-x}Mg_xO_3$) monoliths with macropore frameworks from single-source layered double hydroxide (LDH) precursors. The synthesis strategy mainly involves the formation of sintered two-phase (desired complex metal oxide and MgO phases) composite monoliths and followed selective leaching of self-generated MgO sacrificial template from the composite monoliths, without using any adscititious and prestructured template or structure-directing agents. By adjusting the synthesis parameters such as sintering temperatures and compositions of precursors, the microstructures of monoliths, especially morphologies, particle sizes, spacing among particles, and compositions, could be finely controlled. Moreover, as-prepared $MgAl_2O_4$, $MgFe_2O_4$, and $In_{2-x}Mg_xO_3$ monoliths exhibit promising surface superhydrophobic, ferromagnetic, and semiconductor optical properties, respectively.

Most importantly, the synthetic approach can be flexibly extended to fabricate a broad variety of macroporous complex metal oxides monoliths like AB_2O_4-type spinels ($A = Zn^{2+}, Ni^{2+}$; $B = Al^{3+}, Fe^{3+}, Ga^{3+}, Cr^{3+}$) as long as the sacrificial metal oxide templates (ZnO, NiO, and so on) self-generated during the sintering of precursors is selectively leached from the sintered precursors. This synthesis route described shows the advantage of ease, flexibility, and versatility for fabricating complex metal oxide monolith materials with macropore systems and opens up the possibility of promising applications for such materials as microdevices in diverse areas.

Acknowledgment. The authors gratefully acknowledge the financial support from the National Science Foundation of China, Program for Changjiang Scholars and Innovative Research Team in University (PCSIRT 0406), 111 Project (B07004), and the Program for New Century Excellent Talents in University (NCET-04-0120).

Supporting Information Available: FT-IR spectra of Mg–Al, Mg–Fe, and Mg–In LDH precursors (Figure S1), EDS spectrum of M-3In-1000 monolith (Figure S2), N_2 sorption isotherms of monolith materials (Figure S3), powder XRD patterns of sintered precursors and resultant monoliths (Figure S4), and Tauc plot of $In_{2-x}MgO_3$ monoliths (Figure S5). This material is available free of charge via the Internet at http://pubs.acs.org.

CM702309E

---

(40) (a) Alam, M. J.; Cameron, D. C. *Thin Solid Films* **2000**, *377–378*, 455. (b) Fallaha, H. R.; Ghasemia, M.; Hassanzadehb, A.; Steki, H. *Physica B* **2006**, *373*, 274.

(41) Tang, Q.; Zhou, W.; Zhang, W.; Ou, S.; Jiang, K.; Yu, W.; Qian, Y. *Cryst. Growth Des.* **2005**, *5*, 147.

(42) Peng, X. S.; Meng, G. W.; Wang, X. F.; Wang, Y. W.; Zhang, J.; Liu, X.; Zhang, L. D. *Chem. Mater.* **2002**, *14*, 4490.

(43) Ohhata, Y.; Shinoki, F.; Yoshida, S. *Thin Solid Films* **1979**, *59*, 255.

(44) (a) Liu, Q.; Lu, W.; Ma, A.; Tang, J.; Lin, J.; Fang, J. *J. Am. Chem. Soc.* **2005**, *127*, 5276. (b) Lee, C. H.; Kim, M.; Kim, T.; Kim, A.; Paek, J.; Lee, J. W.; Choi, S.-Y.; Kim, K.; Park, J.-B.; Lee, K. *J. Am. Chem. Soc.* **2006**, *128*, 9326. (c) Zhao, Y.; Zhang, Z.; Wu, Z.; Dang, H. *Langmuir* **2004**, *20*, 27. (d) Wu, X. C.; Hong, J. M.; Han, Z. J.; Tao, Y. R. *Chem. Phys. Lett.* **2003**, *373*, 28. (e) Liang, C.; Meng, G.; Lei, Y.; Phillipp, F.; Zhang, L. *Adv. Mater.* **2001**, *13*, 1330.

(45) Kim, J. S.; Kang, H. I.; Kim, W. N.; Kim, J. I.; Choi, J. C.; Park, H. L.; Kim, G. C.; Kim, T. W.; Hwang, Y. H.; Mho, S. I.; Jung, M.-C.; Han, M. *Appl. Phys. Lett.* **2003**, *82*, 2029.